Scripta Materialia 277 (2026) 117228

Contents lists available at ScienceDirect

Scripta Materialia

journal homepage: www.journals.elsevier.com/scripta-materialia

Discovery of novel phenomenon and mechanism revelation of an Al-Zn-Mg-Cu alloy without intergranular corrosion

Mengxia Han [a,1], Sida Liu [b,*], Lei Zhang [c], Weikang Wu [a], Guiliang Liu [a,d], Ge Wu [e,*], Weiyi Wang [a,*], Xiangfa Liu [a,*]

[a] Key Laboratory for Liquid-Solid Structural Evolution and Processing of Materials, Ministry of Education, Shandong University, Jinan 250061, China
[b] Laboratory for multiscale mechanics and medical science, SV LAB, School of Aerospace, Xi'an Jiaotong University, Xi'an 710049, China
[c] School of Chemistry and Chemical Engineering, Shandong University, Jinan 250061, China
[d] Shandong Crystal Seed Materials Co., Ltd, Linyi 276400, China
[e] Center for Advancing Materials Performance from the Nanoscale (CAMP-Nano) and Hysitron Applied Research Center in China (HARCC), State Key Laboratory for Mechanical Behavior of Materials, Xi'an Jiaotong University, Xi'an, China

ARTICLE INFO

Keywords:
Al-Zn-Mg-Cu alloys
Intergranular corrosion
Grain boundary precipitates
First-principles calculations
Molecular dynamics simulations

ABSTRACT

This study identified an unreported phenomenon where the Al-8.8Zn-2Mg-2Cu alloy exhibit no intergranular corrosion in 5.7% NaCl+0.3% H_2O_2 solution, which could be attributed to the formation of dispersive $MgZn_2$ phase along grain boundaries. Compared with the $Mg_2Al_4Zn_3$ grain boundary precipitates in Al-6.6Zn-2Mg-2Cu alloy, $MgZn_2$ demonstrates a stronger electron localization tendency, indicating superior bonding capability and structural stability. The lower density of states value near Fermi energy level suggests reduced susceptibility to electron transfer of $MgZn_2$ compared with $Mg_2Al_4Zn_3$. Combined with adsorption energy, corrosive solution tends to accumulate preferentially on Al phase in Al-8.8Zn-2Mg-2Cu alloy, while it distributes relatively uniformly across both $Mg_2Al_4Zn_3$ and Al phases in Al-6.6Zn-2Mg-2Cu alloy. Thus, corrosion propagates along $Mg_2Al_4Zn_3$ phases at grain boundaries, leading to severe intergranular corrosion. Conversely, $MgZn_2$ exhibits corrosion resistance similar to Al, and corrosive medium accumulation on $MgZn_2$ is less favored, which suppresses the initiation of intergranular corrosion at source.

Over the past decade, related research has focused on the mechanical properties enhancement of Al-Zn-Mg-(Cu) alloys without compromising their corrosion resistance, to improving the service stability in aerospace structural components [1,2]. Conventional wisdom states that increasing the content of main alloying elements, especially Zn, can increase the number density of aging precipitates, as exemplified by the evolution of 7050 to 7055 alloys, followed by 7A93 alloys. However, with the degree of alloying, the resistance to pitting corrosion (PC) and intergranular corrosion (IGC) significantly deteriorates [3–5]. Generally, the IGC resistance of Al-Zn-Mg-Cu alloys is closely related to the composition and distribution of grain boundary precipitates (GBPs), which can act as anodes and are preferentially corroded, leading to the initiation and propagation of IGC cracks [6–8]. The degree of corrosion can also become more severe with more continuous distribution of these precipitates [9]. Some studies have suggested that impurity phases, such as Al_7Cu_2Fe particles, can induce pitting corrosion and further facilitate the ingress of corrosive media into the interior of alloy due to their poorly protective oxide film and galvanic corrosion with Al matrix. The occur of pitting corrosion further induces and promotes IGC [10,11], which has been also observed in other systems such as Al-Mg-Si and Al-Cu-Mg alloys [12,13]. In this study, a novel phenomenon is discovered that the Al-8.8Zn-2Mg-2Cu alloy with high content of Zn and impurity Al_7Cu_2Fe phase does not mean a decrease of IGC resistance. On the contrary, IGC does not occur in NaCl+H_2O_2 solution. The underlying mechanisms have been elucidated through a combination of experimental validation and computational modeling, offering new strategies for the development of ultra-high strength and corrosion-resistant aluminum alloys.

Three alloys were designed, with the chemical composition presented in Supplementary Materials Table 1, denoted as A, B and C,

* Corresponding authors.
E-mail addresses: hanmengxia1126@163.com (M. Han), sidaliu@xjtu.edu.cn (S. Liu), gewuxjtu@xjtu.edu.cn (G. Wu), wangweiyi@sdu.edu.cn (W. Wang), xfliu@sdu.edu.cn (X. Liu).
[1] First author

https://doi.org/10.1016/j.scriptamat.2026.117228
Received 14 November 2025; Received in revised form 9 February 2026; Accepted 10 February 2026
Available online 14 February 2026
1359-6462/© 2026 Acta Materialia Inc. Published by Elsevier Inc. All rights are reserved, including those for text and data mining, AI training, and similar technologies.

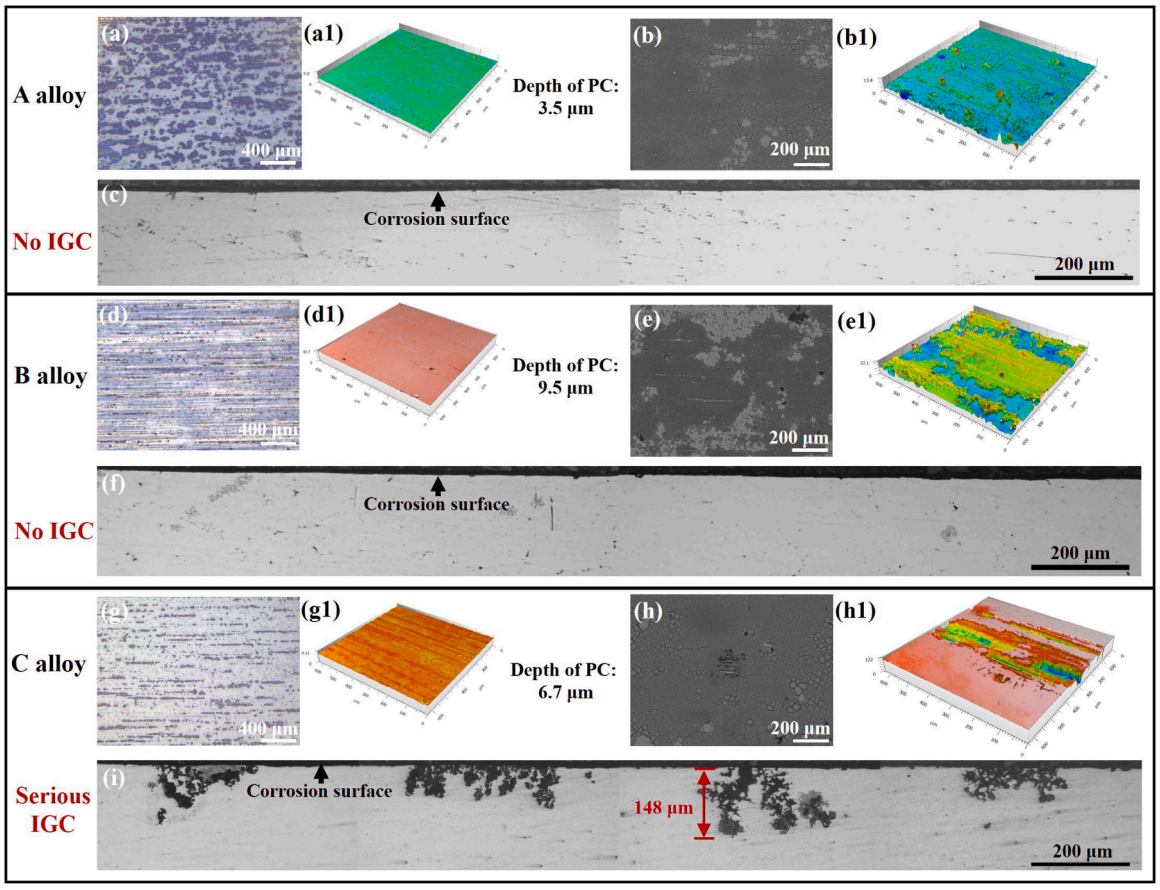


Fig. 1. Corrosion morphology of the alloys in different solutions: (a, a1), (d, d1), (g, g1) the OM and CLSM morphologies of corrosion surface of A, B and C alloys immersed in NaCl aqueous solution, respectively, (b, b1), (e, e1), (h, h1) the OM and CLSM morphologies of corrosion surface of A, B and C alloys immersed in NaCl+H_2O_2 aqueous solution, respectively, (c, f, i) the IGC morphology of the cross section of A, B and C alloys, respectively.

corresponding to Al-8.8Zn-2Mg-2Cu-0.01Fe, Al-8.8Zn-2Mg-2Cu-0.14Fe and Al-6.6Zn-2Mg-2Cu-0.01Fe alloys. Given that the addition of TCB seed alloy significantly enhanced the corrosion resistance of the alloys in our previous studies, A, B and C alloys in this work were added with 0.5 % (wt. %, the same below) Al-TCB seed alloy [14,15]. All the raw materials were supplied by Shandong Crystal Seed Materials Co., Ltd. For

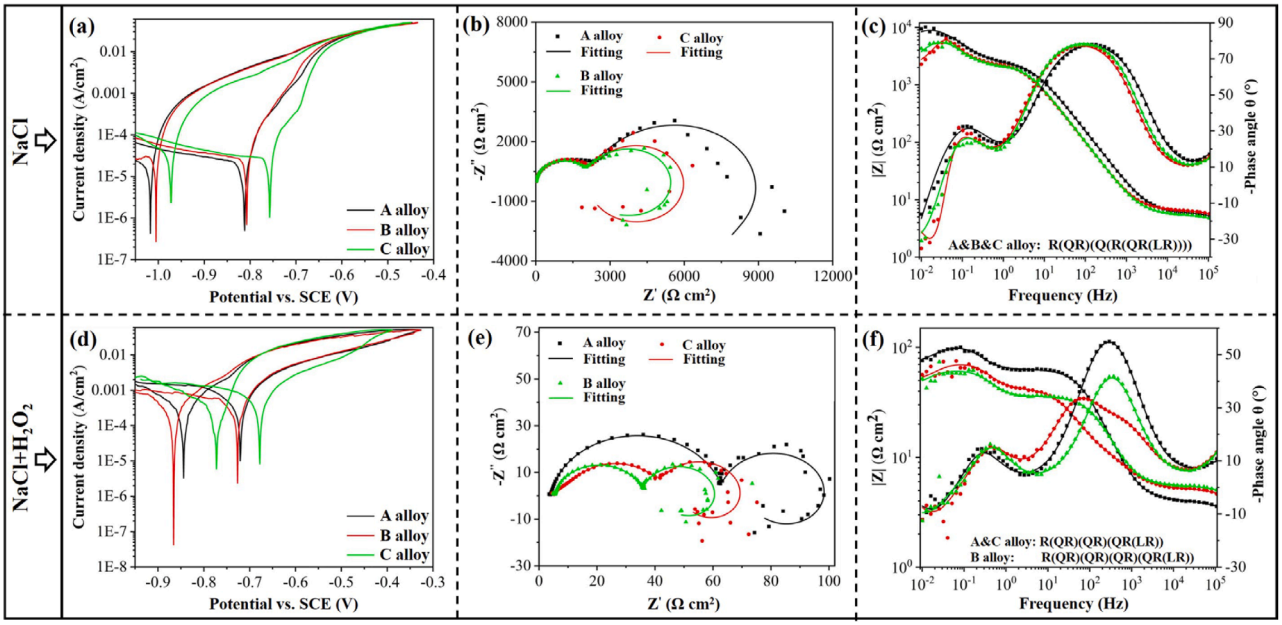


Fig. 2. Electrochemical testing results of the alloys in different solutions: (a-c) CP curve, Nyquist and Bode plots in NaCl aqueous solution, (d-f) CP curve, Nyquist and Bode plots in NaCl+H_2O_2 aqueous solution.

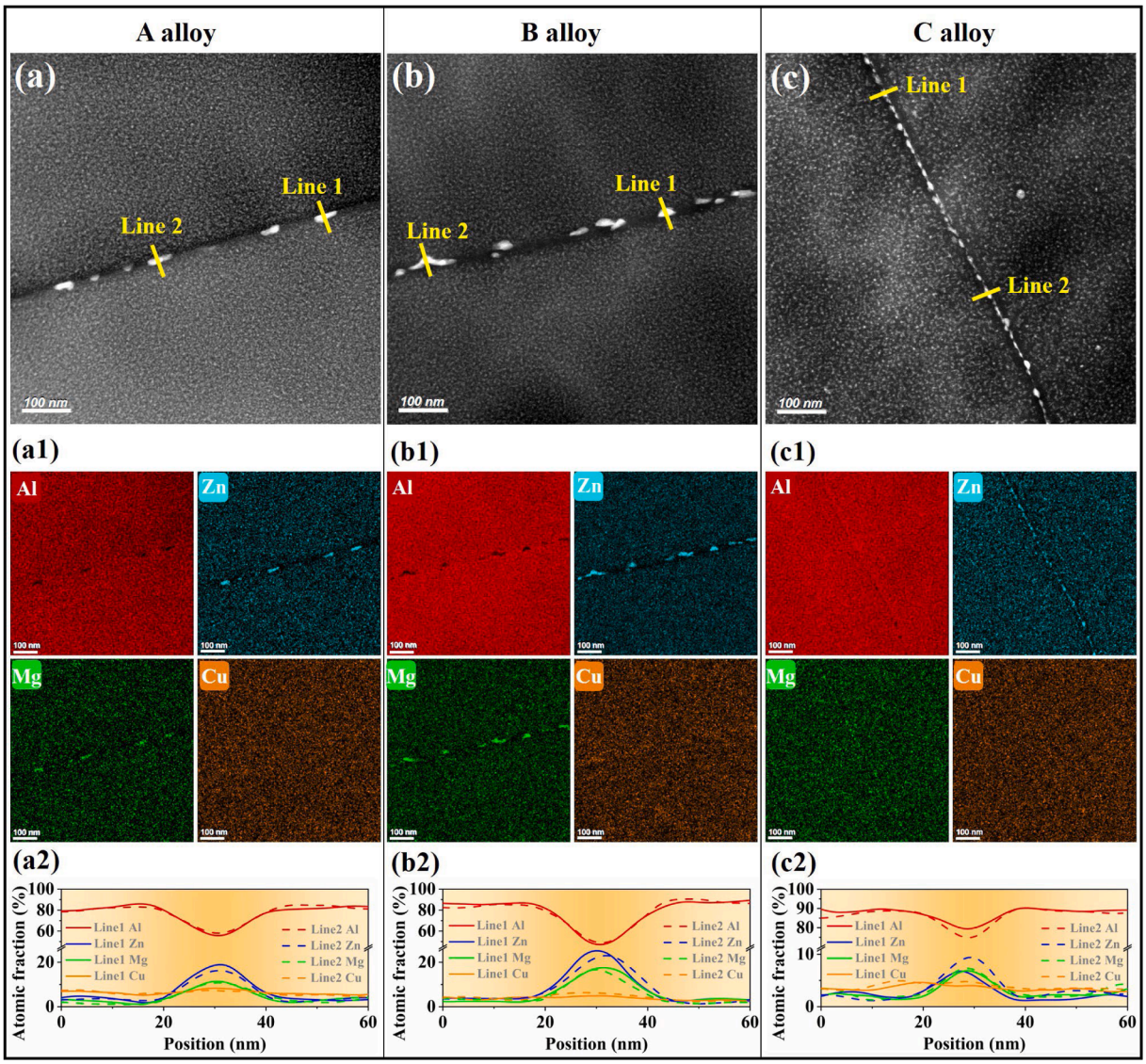


Fig. 3. The characteristic of grain boundary precipitates in the alloys. A alloy: (a, a1) HAADF-STEM image and its EDS mapping analysis, (a2) EDS lining analysis of line 1&2 in figure (a). B alloy: (b, b1, b2) description as set forth for A alloy. C alloy: (c, c1, c2) description as set forth for A alloy.

the casting process, the alloys were poured into the graphite cylinder (Φ90 mm) at 720 °C. After homogenized at 465 °C for 24 h, the alloys were hot extruded into round rods with a diameter of 20 mm. Then solution and aging treatments (T6, 475 °C/1h+120 °C/24 h) were conducted, which were used for immersion corrosion and electrochemical tests.

Two typical corrosion environments were established, including (I) immersion in 3.5 % NaCl aqueous solution for 72 h, (II) immersion in an aqueous solution of 57 g/L NaCl+10 mL/L H_2O_2 (i.e., 5.7 % NaCl+0.3 % H_2O_2) for 6 h. All corrosion tests were conducted at 30±1 °C. Cyclic polarization (CP) and electrochemical impedance spectroscopy (EIS) tests were conducted on the above solution. The test parameters can be found in our previous studies [14–16]. Optical microscopy (OM, DM 2700 M), scanning electron microscopy (SEM, JSM 7800F) and confocal laser scanning microscopy (CLSM, LSM 800) were employed to analyze the corrosion morphology. Analysis of GBPs was carried out using a transmission electron microscopy (TEM, Talos F200X) equipped with a high-resolution energy dispersive spectrometer (EDS). First-principles calculations based on density functional theory (DFT) were performed by the VASP including electron localization function (ELF), density of states (DOS), work function (WF), differential charge density (DCD) of GBPs, while molecular dynamics (MD) simulations using by LAMMPS package were employed to calculate the adsorption energy between GBPs/Al and corrosion solution. The detailed parameters were provided in the Supplementary Materials.

The corrosion morphologies of the three alloys in different corrosion environments are shown in Fig. 1. As shown in Fig. 1 (a, d, g), only PC with similar morphology can be observed on all the alloys in the NaCl solution, with corrosion pits distributes along the extrusion direction. Among them, severe galvanic corrosion occurs between this phase and Al matrix [17] due to the presence of numerous Al_7Cu_2Fe phases in alloy B (Fe content 0.138 %), resulting in the deepest pit depth of 9.5 μm (Fig.1(d1)). The deepest pits of A and C alloys are 3.5 μm and 6.7 μm, respectively (Fig.1 (a1, g1)). In the NaCl+H_2O_2 solution, both A and B alloys did not undergo IGC (Fig. 1(c, f)), while C alloy experienced severe IGC (Fig. 1(i)), with the maximum depth reaching 148 μm. Relatively large oxide films formed on the surfaces of all alloys. Particularly, a relatively intact oxide film is observed around the Al_7Cu_2Fe particles in B alloy (Fig.1(e)), with no significant galvanic corrosion, indicating that the Al_7Cu_2Fe phase could not induce IGC. In summary, in the NaCl solution, the PC behaviors of the three alloys are similar, with pit depths generally within the same order of magnitude. However, in the

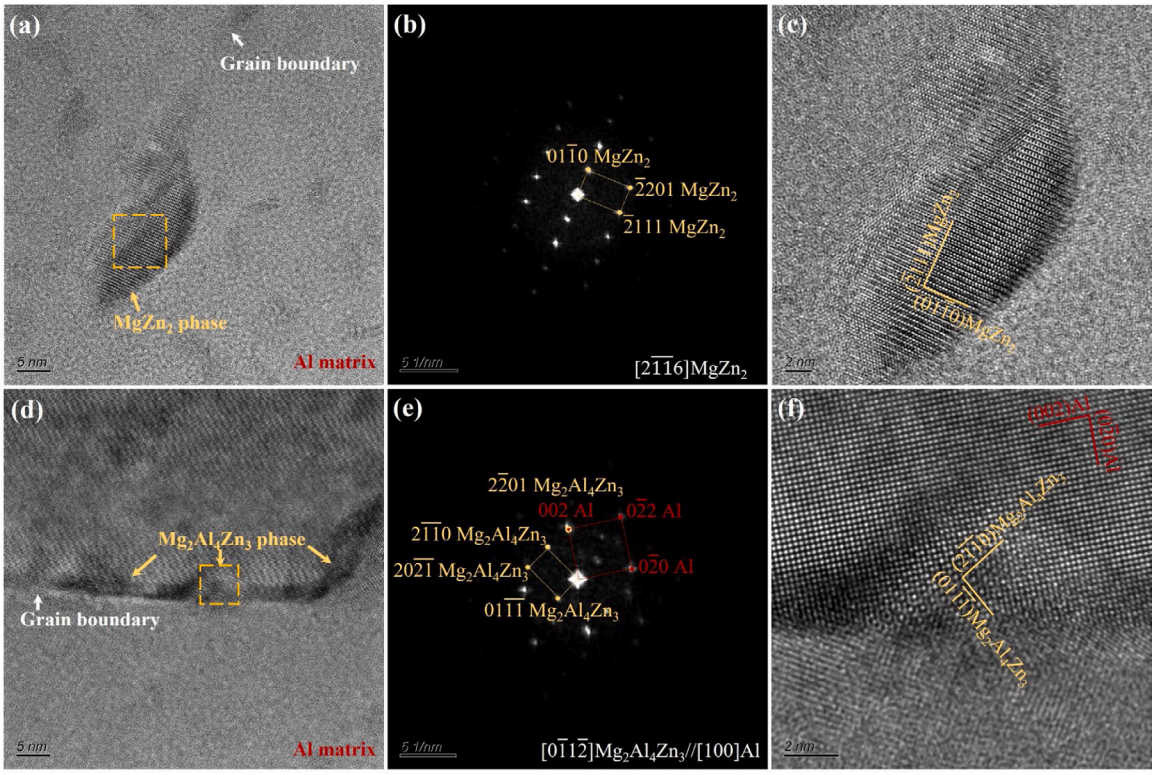


Fig. 4. HRTEM analyses of grain boundary precipitates in A and C alloys: (a, b) HRTEM and the corresponding FFT image of dashed box in figure (a) of A alloy, (c) high magnification HRTEM image; (d, e) HRTEM and the corresponding FFT image of dashed box in figure (d) of C alloy, (f) high magnification HRTEM image.

NaCl+H_2O_2 solution, A and B alloys with higher content of Zn demonstrate excellent resistance to IGC. The Fe contents are 0.013 %, 0.138 % and 0.011 % for A, B and C alloys, while the Zn contents are 8.83 %, 8.79 % and 6.64 %, respectively. It indicates that the Fe content has no effect on IGC in this study, rather, it is the Zn content that exerts the fundamental influence.

Fig. 2 shows the CP and EIS testing results of the three alloys in different corrosive environments, with relevant parameters provided in Supplementary Materials Table 2 and Table 3. The CP results indicate that, compared with C alloy, A and B alloys exhibit lower I_{corr} and higher E_{sw}-E_{corr} values in both NaCl and NaCl+H_2O_2 solutions, demonstrating that the A and B alloys with higher Zn have a slower corrosion rate and mitigated corrosion degradation in these two corrosive environments [18–20]. Notably, in the NaCl+H_2O_2 solution, C alloy does not show an E_{ptp} value, indicating that the localized corrosion processes such as PC and IGC cannot self-repair. According to the EIS testing result, all three alloys exhibit capacitive arcs in the high and medium frequency regions, while inductive arcs are observed in the low frequency region. This indicates that the corrosion behavior at the interface between alloy surface and corrosive solution involves both the oxide film and the alloy itself, corresponding to two time-constants. Although the fitting current includes three constant phase elements, the initial time-constant in the high frequency region represents the electrochemical characteristics of the instrument and connecting wires, which has no practical significance [7,19,21,22]. The appearance of inductive arc in the low frequency region suggests the initiation and growth of metastable or stable PC [23–26]. In the NaCl+H_2O_2 solution, it also includes the initiation and propagation of IGC. In the NaCl solution, compared with C alloy, A and B alloys exhibit higher R_{ct} and R_f values, indicating that the two alloys own higher polarization resistance. Furthermore, the connection mode of such constant phase elements in the circuit demonstrates that, the corrosion medium attacks the oxide film and alloy in a certain sequence of time from earlier to later in the NaCl solution. While in the NaCl+H_2O_2 solution, the corrosion process occurs almost simultaneously on both the oxide film and the alloy based on the connection mode of the two constant phase elements. Additionally, Bode plot of the B alloy exhibits three peaks, fitted using three constant phase elements, respectively. This suggests that the oxide film structure of the alloy is relatively complex, with significant differences between the naturally formed oxide film and the corrosion induced oxide film. As a result, these two types of films can be considered to coexist on the alloy surface, which may be attributed to the presence of Al_7Cu_2Fe phase. In the NaCl+H_2O_2 solution, A and B alloys still exhibit higher R_{ct} and R_f values compared to C alloy, which indicates that at more vulnerable locations such as grain boundaries, the alloy and oxide film can resist the attack of corrosive medium more effectively, and inhibit the occurrence of IGC. Therefore, the electrochemical analyses further corroborate the findings mentioned above, demonstrating that A and B alloys with higher content of Zn exhibit excellent IGC resistance in the NaCl+H_2O_2 solution.

To elucidate the mechanism for the excellent IGC resistance of the alloys with higher content of Zn mentioned above, TEM and EDS analyses was conducted on the characteristics of GBPs in the three alloys. As shown in Fig. 3(a, b, c), no obvious precipitate free zones are observed in the three alloys. However, the distribution of GBPs in A and B alloys is relatively discontinuous, while that in C alloy exhibits a more continuous characteristic. From the compositional perspective, the GBPs in all three alloys primarily contained Mg and Zn elements (Fig. 3(a1, b1, c1)), while extensive statistical analysis reveals differences in their compositional ratios. The Zn/Mg ratio in A and B alloys is approximately 1.7–1.9, close to that of the typical aging precipitate $MgZn_2$ [27,28]. In contrast, the Zn/Mg ratio in C alloy is approximately 1.0–1.4, with a higher content of Al, approaching that of the typical aging precipitate $Mg_2Al_4Zn_3$ [29–31]. Therefore, the characteristics of GBPs clearly play a critical role in influencing the IGC behavior of the alloys.

To further determine the crystal structures of the two grain boundary precipitates, high-resolution TEM (HRTEM) analysis and the corresponding fast Fourier transforms (FFT) were performed on A and C

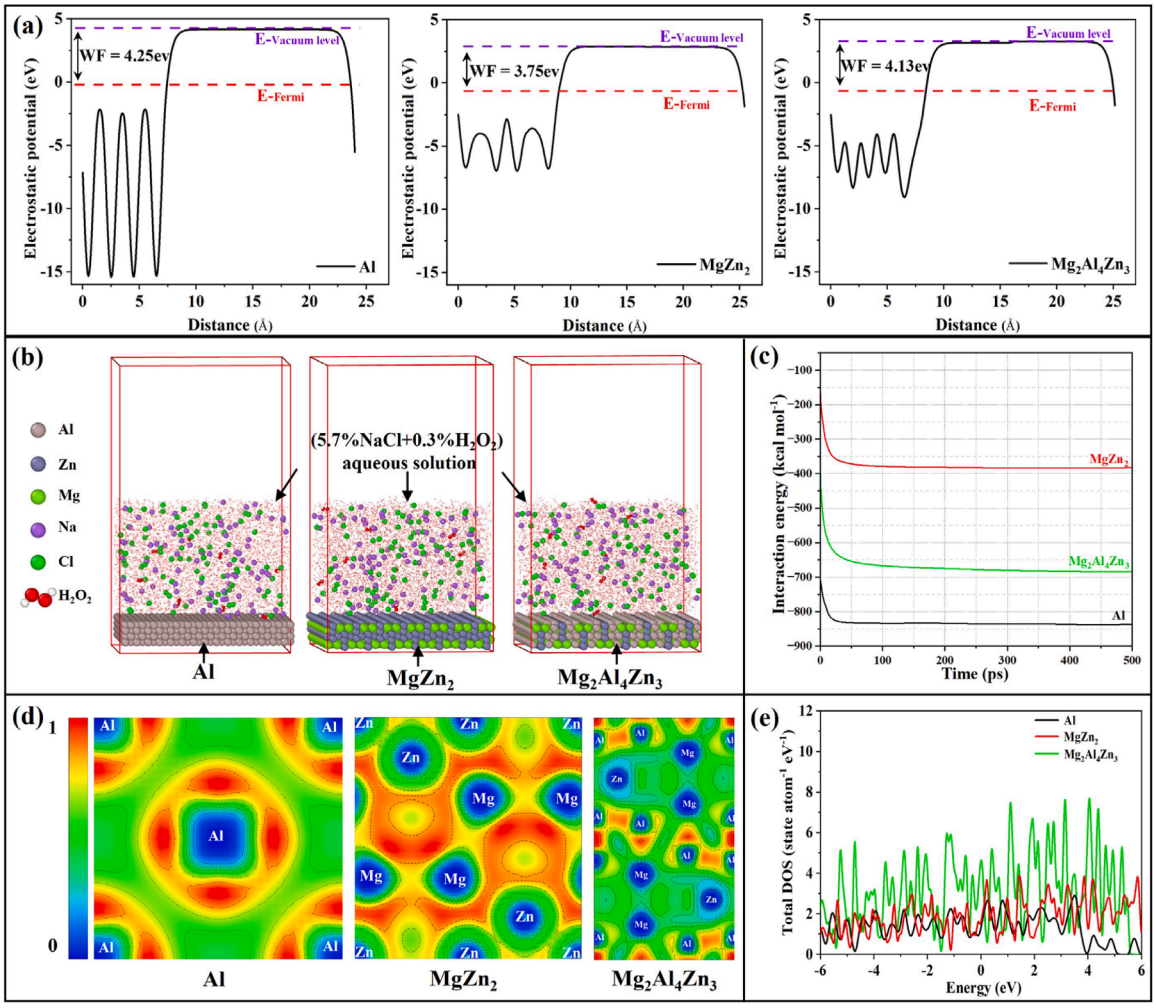


Fig. 5. The DFT and MD calculation results of Al, $MgZn_2$ and $Mg_2Al_4Zn_3$ phases: (a) WF, (b) The MD modeling of the phases in (5.7 %NaCl+0.3 %H_2O_2) aqueous solution corrosion environment, in which (100) Al, (10$\bar{1}$0) $Mg_2Al_4Zn_3$ and (10$\bar{1}$0) $MgZn_2$ are in contact with the solution, and the adsorption energy of such phases in solid-liquid system displayed in figure (c), (d) 2D ELF cut plane, (e) Total DOS.

alloys, as shown in Fig. 4. The crystal structures of the two grain boundary precipitates are different. Indexing the FFT diffraction spots of the grain boundary precipitate in A alloy reveals that it corresponds to the structure of the $MgZn_2$ phase, consistent with mp-1124 material from the Materials Project database [32]. Similarly, indexing the FFT spots of the grain boundary precipitate in C alloy indicates that it matches the structure of the $Mg_2Al_4Zn_3$ phase, in agreement with the mp-1189,454 material from the same database [33]. The crystallographic parameters of both phases are provided in the Supplementary Materials, which is used for modeling and calculation.

Based on the above analysis, two typical aging precipitates, $MgZn_2$ and $Mg_2Al_4Zn_3$, as well as Al were first modeled (Fig. 1 and crystal structure of $MgZn_2$ and $Mg_2Al_4Zn_3$ in Supplementary Materials), and first-principles calculations based on DFT were performed to reveal their intrinsic characteristics. As shown in Fig. 5(a), the WF values of both $MgZn_2$ and $Mg_2Al_4Zn_3$ phases are lower than that of Al, indicating that both phases tend to act as anodes in galvanic corrosion and are preferentially attacked [34,35]. Corrosion behavior occurs in a corrosive medium, with the interaction between these phases and medium environment considered crucial, serving as the dominant factor determining the corrosion tendency. Thus, a corrosive environment with the same concentration as the actual IGC solution, i.e., (5.7 % NaCl + 0.3 % H_2O_2) aqueous solution was constructed, and the solid-liquid system models were established (Fig. 5(b)). For crystallographic plane selected for exposure to the corrosive solution, the most stable low-index surfaces for each phase were used, the Al is (100), the $Mg_2Al_4Zn_3$ and $MgZn_2$ are (10$\bar{1}$0). MD simulations were then performed to calculate the adsorption energy of this solution on the surfaces of such second phases [36,37]. The results are shown in Fig. 5(c). Judging from the adsorption energy values, $MgZn_2$ phase has the weakest adsorption energy relative to the corrosive solution, $Mg_2Al_4Zn_3$ phase ranks second, and the Al phase has the strongest adsorption energy relative to the corrosive solution. In comparison, for the system composed of $MgZn_2$ and Al phases, the difference in adsorption energy is 460 kcal·mol^{-1}, while for the system composed of $Mg_2Al_4Zn_3$ and Al phases, the adsorption energy difference is only 160 kcal·mol^{-1}. Considering the significant difference in adsorption energy values, in the former system, the corrosive solution tends to preferentially accumulate on the surface of Al phase, whereas in the latter, the corrosive solution distributes relatively uniformly on the surfaces of both the $Mg_2Al_4Zn_3$ and Al phases. Therefore, in systems composed with the Al matrix and one of the second phases, the interaction between $MgZn_2$ phase and the corrosive medium is very weak, while the interaction between $Mg_2Al_4Zn_3$ phase and the corrosive medium is relatively strong. In addition, the intrinsic characteristics of the phases, namely their bonding capability and structural stability, should be considered, as these are also key factors influencing the corrosion behaviors. First, the analysis of ELF is shown in Fig. 5(d). For Al phase, the ELF value in the Al-Al bond region is approximately 0.5, indicating a delocalized state of valence electrons, which reflects the typical metallic

bonding nature. In $MgZn_2$ phase, high ELF values appear in Mg-Mg and Mg-Zn bond regions, suggesting a strong tendency for valence electrons to localize. This electron distribution indicates that the bonding in $MgZn_2$ exhibits certain covalent characteristics. For $Mg_2Al_4Zn_3$ phase, some electrons still demonstrate strong delocalization features, such as in the Mg-Mg and Al-Zn bond regions, which exhibits metallic bonding characteristics, while certain localized Al-Mg regions show covalent components based on ELF values. Therefore, the $MgZn_2$ phase exhibits stronger bonding capability and superior structural stability compared to the $Mg_2Al_4Zn_3$ phase [38]. Generally, the electron transfer rate in the double electric layer is proportional to the DOS of the phase, which can be used to evaluate corrosion resistance from the perspective of corrosion kinetics [38,39]. This is because, during the corrosion process, valence electrons near the Fermi level are readily transferred to ions in the solution. Therefore, the DOS near the Fermi level determines the electrochemical activity, i.e., a higher DOS near the Fermi level facilitates the charge transfer process in electrochemical reactions. Thus, the DOS of $MgZn_2$, $Mg_2Al_4Zn_3$ and Al phases were calculated. The Fermi level was set to zero on the energy axis, which is the highest energy level occupied by electrons in the band structure at absolute zero (0 K). The results (Fig. 5(e)) show that $Mg_2Al_4Zn_3$ has the highest DOS value near the Fermi level, while the values of $MgZn_2$ and Al are close to each other. This indicates that the charge transfer process encounters the least resistance for $Mg_2Al_4Zn_3$, indicating that it is more susceptible to corrosive dissolution. By contrast, the DOS values near the Fermi level for $MgZn_2$ and Al are similar, suggesting that $MgZn_2$ is less prone to corrosive dissolution compared with $Mg_2Al_4Zn_3$.

In summary, a previously unreported phenomenon was presented in this study. The Al-8.8Zn-2Mg-2Cu alloy with higher content of Zn exhibits no IGC in a (5.7 % NaCl+0.3 % H_2O_2) aqueous solution, whereas the Al-6.6Zn-2Mg-2Cu alloy with lower content of Zn demonstrates typical IGC behavior, with a maximum depth reaching 148 μm. Electrochemical test results further confirm this phenomenon. TEM analysis reveals that the GBPs in the former are relatively dispersed $MgZn_2$ phase, while in the latter, they are relatively continuous $Mg_2Al_4Zn_3$ phase. Therefore, DFT calculations and MD simulations were employed to analyze the intrinsic characteristics of the $MgZn_2$ and $Mg_2Al_4Zn_3$ phases and their interactions with the corrosive medium. The WF values indicate that both the $MgZn_2$ and $Mg_2Al_4Zn_3$ phases tend to act as anodes and are preferentially corroded in galvanic corrosion. However, based on the MD simulations, for the system composed of $MgZn_2$ and Al phases, the corrosive solution tends to preferentially accumulate on the surface of Al phase, whereas in the system composed of $Mg_2Al_4Zn_3$ and Al, the corrosive solution distributes relatively uniformly on the surfaces of both the $Mg_2Al_4Zn_3$ and Al phases. That is, the interaction between $MgZn_2$ and corrosive medium is much weaker than that of $Mg_2Al_4Zn_3$. As indicated by the ELF analysis, compared with $Mg_2Al_4Zn_3$, $MgZn_2$ exhibits enhanced bonding capability and greater structural stability. Meanwhile, the lower DOS value of $MgZn_2$ near the Fermi level suggests a lower propensity for charge transfer and dissolution by corrosive solution. According to the above analyses, the $MgZn_2$ phase demonstrates superior corrosion resistance compared to the $Mg_2Al_4Zn_3$ phase, and is not susceptible to be attacked in a NaCl+H_2O_2 environment. This finding provides theoretical guidance for designing the composition and heat treatment processes of Al-Zn-Mg-Cu series alloys with enhanced IGC resistance.

CRediT authorship contribution statement

Mengxia Han: Writing – original draft, Software, Formal analysis, Conceptualization. **Sida Liu:** Writing – review & editing, Supervision. **Lei Zhang:** Data curation. **Weikang Wu:** Software. **Guiliang Liu:** Resources. **Ge Wu:** Formal analysis, Data curation. **Weiyi Wang:** Writing – review & editing, Funding acquisition, Formal analysis, Data curation. **Xiangfa Liu:** Writing – review & editing, Resources, Methodology, Funding acquisition.

Declaration of competing interest

The authors declare that they have no known competing financial interests or personal relationships that could have appeared to influence the work reported in this paper.

Acknowledgements

This work was supported financially by the National Natural Science Foundation of China (Nos. U2241230, 52404406, U24A2026), the Key R&D Program of Shandong Province (No. 2023CXGC010309), the Natural Science Foundation of Shandong Province (No. ZR2024QE412) and the Young Scholars Program of Shandong University.

Supplementary materials

Supplementary material associated with this article can be found, in the online version, at doi:10.1016/j.scriptamat.2026.117228.

References

[1] J. Wang, F. Li, Research status and prospective properties of the Al-Zn-Mg-Cu series aluminum alloys, Metals 13 (8) (2023) 1329.
[2] A. Azarniya, A.K. Taheri, K.K. Taheri, Recent advances in ageing of 7xxx series aluminum alloys: a physical metallurgy perspective, J. Alloys Compd. 781 (2019) 945–983.
[3] D. Yuan, S. Chen, K. Chen, L. Huang, J. Chang, L. Zhou, Y. Ding, Correlations among stress corrosion cracking, grain-boundary microchemistry, and Zn content in high Zn-containing Al-Zn-Mg-Cu alloys, T. Nonferr. Metal. Soci. 31 (8) (2021) 2220–2231.
[4] C. Li, X. Xu, H. Chen, V. Tabie, J. Cai, Y. Liu, Z. Liu, C. Peng, Effect of Zn/Mg ratio on microstructure and properties of cold extruded Al-xZn-2.4Mg-0.84Cu-0.2Zr-0.25Ti aluminum alloy, J. Mater. Eng. Perform. 29 (9) (2020) 5787–5795.
[5] Y.H. Jo, H. Jung, S. Jeon, H. Choi, H.-W. Kim, H. Sung, The effect of Zn content on tensile properties and fracture toughness of Al-Zn-Mg-Cu alloy, J. Mater. Res. Technol. 36 (2025) 5696–5706.
[6] C.K. Akuata, O. Beyß, L.T. Belkacemi, K. Hantzsche, M.E. Curd, D. Zander, On the impact of Cr and Ag additions on the grain boundary microchemistry, hydrogen permeability and environmentally assisted cracking mechanism of an Al-Zn-Mg-Cu-Zr 7xxx alloy, Corros. Sci. 246 (2025) 112759.
[7] J. Li, T. He, X.-Y. Du, A. Vereschaka, Enhancing the corrosion resistance of high-strength Al-Zn-Mg-Cu alloys after equal channel angular pressing by developing retrogression and re-aging strategies, Corros. Sci. 246 (2025) 112736.
[8] F. Guo, S. Duan, Y. Pan, D. Wu, K. Matsuda, T. Wang, Y. Zou, Stress corrosion behavior and microstructure analysis of Al-Zn-Mg-Cu alloys friction stir welded joints under different aging conditions, Corros. Sci. 210 (2023) 110821.
[9] H.C. Fang, H. Chao, K.H. Chen, Effect of recrystallization on intergranular fracture and corrosion of Al-Zn-Mg-Cu-Zr alloy, J. Alloys Compd. 622 (2015) 166–173.
[10] Y. Sun, Z. Wang, Q. Pan, W. Chen, Z. Yin, D. Li, Q. Zheng, Localized corrosion process of Al-Zn-Mg-Cu-Zr alloy: transitions from pitting corrosion to intergranular corrosion, J. Central South Univ. 30 (7) (2023) 2120–2132.
[11] W. Xue, Y. Wang, S. Wu, B. Zhang, Z. Zhang, X. Zhuo, P. Zuo, S. Lu, J. Xia, X. Li, J. Wu, Influence of impurity content on corrosion behavior of Al-Zn-Mg-Cu alloys in a tropical marine atmospheric environment, Corros. Sci. 237 (2024) 112319.
[12] V. Guillaumin, G. Mankowski, Localized corrosion of 6056 T6 aluminium alloy in chloride media, Corros. Sci. 42 (2000) 105–205.
[13] X. Zhang, X. Zhou, T. Hashimoto, B. Liu, Localized corrosion in AA2024-T351 aluminium alloy: transition from intergranular corrosion to crystallographic pitting, Mater. Charact. 130 (2017) 230–236.
[14] W. Wang, M. Han, G. Liu, Q. Sun, H. Duan, X. Liu, A new insight to regulate microstructure and enhance corrosion resistance of the Al-Mg-Si alloy by TCB seed alloy, Mater Des 251 (2025) 113654.
[15] M. Han, W. Wang, G. Liu, X. Liu, The enhance of Al-TCB seed alloy on the corrosion resistance of 7050 alloy by multi-level structures modification, J. Mater. Res. Technol. 36 (2025) 3213–3226.
[16] W.Y. Wang, Q.L. Pan, X.D. Wang, J. Ye, Z.Q. Huang, S.Q. Xiang, B. Liu, Effect of laser shock peening on corrosion behaviors of ultra-high strength Al-Zn-Mg-Cu alloys prepared by spray forming and ingot metallurgy, Corros. Sci. 205 (2022) 110458.
[17] J.C. Li, J. Dang, A summary of corrosion properties of Al-rich solid solution and secondary phase particles in Al alloys, Metals 7 (3) (2017) 84.
[18] C. Han, M. Yu, J. Xiao, Z. Yang, Z. Zhao, X. Jia, S. Li, J. Liu, Effect and mechanism of Li content on the corrosion resistance of Al-Li alloy, Corros. Sci. 246 (2025) 112768.
[19] F. Ozdemir, C.S. Witharamage, J. Christudasjustus, A.A. Darwish, H. Okuyucu, R. K. Gupta, Corrosion behavior of a bulk nanocrystalline Al-Fe alloy, Corros. Sci. 209 (2022) 110727.
[20] U. Trdan, T. Sano, D. Klobcar, Y. Sano, J. Grum, R. Sturm, Improvement of corrosion resistance of AA2024-T3 using femtosecond laser peening without protective and confining medium, Corros. Sci. 143 (2018) 46–55.

[21] C. Peng, G. Cao, T. Gu, C. Wang, Z. Wang, C. Sun, The effect of dry/wet ratios on the corrosion process of the 6061 Al alloy in simulated Nansha marine atmosphere, Corros. Sci. 210 (2023) 110840.
[22] A.P. Babu, S. Choudhary, J.C. Griffith, A. Huang, N. Birbilis, On the corrosion of a high solute Al-Zn-Mg alloy produced by laser powder bed fusion, Corros. Sci. 189 (2021) 109626.
[23] W. Liu, Q. Li, M.C. Li, Corrosion behaviour of hot-dip Al-Zn-Si and Al-Zn-Si-3Mg coatings in NaCl solution, Corros. Sci. 121 (2017) 72–83.
[24] C. Guo, H.T. Zhang, S.S. Li, R.X. Chen, Y.F. Nan, L. Li, P. Wang, B.M.A. Li, J.Z. Cui, H. Nagaumi, Evolution of microstructure, mechanical properties and corrosion behavior of Al-4Mg-2Zn-0.3Ag (wt.%) alloy processed by T6 or thermomechanical treatment, Corros. Sci. 188 (2021) 109551.
[25] P. Liu, L.L. Hu, Q.H. Zhang, C.P. Yang, Z.S. Yu, J.Q. Zhang, J.M. Hu, F.H. Cao, Effect of aging treatment on microstructure and corrosion behavior of Al-Zn-Mg aluminum alloy in aqueous solutions with different aggressive ions, J. Mater. Sci. Technol. 64 (2021) 85–98.
[26] M. Abeens, R. Muruganandhan, K. Thirumavalavan, Effect of low energy laser shock peening on plastic deformation, wettability and corrosion resistance of aluminum alloy 7075 T651, Optik 219 (2020) 165045.
[27] T. Marlaud, A. Deschamps, F. Bley, W. Lefebvre, B. Baroux, Influence of alloy composition and heat treatment on precipitate composition in Al-Zn-Mg-Cu alloys, Acta Mater 58 (1) (2010) 248–260.
[28] X. Zhang, J. Wang, Atomistic mechanism of η'-to-η transformation in Al-Zn-Mg-Cu alloys, Scripta Mater 231 (2023) 115474.
[29] Y. Wang, D. Freiberg, Y. Huo, W. Zhu, M. Li, R.E.A. Williams, Y. Wang, A combined simulation and experimental study of the equilibrium shapes of η′ and α precipitates in Mn-containing 7xxx Al-alloys, Acta Mater 259 (2023) 119094.
[30] B. Chen, C.H. Zhang, Y. Jin, First-principles study on surface fracture of Al-Zn-Mg-Cu alloy under stress load and H environment, Surf. Interface. 26 (2021) 101366.
[31] F. Cao, J. Zheng, Y. Jiang, B. Chen, Y. Wang, T. Hu, Experimental and DFT characterization of η′ nano-phase and its interfaces in Al Zn Mg Cu alloys, Acta Mater 164 (2019) 207–219.
[32] MgZn2 phase, mp-1124 in The Materials Project. https://next-gen.materialsproject.org/materials/mp-1124?chemsys=Mg-Zn.
[33] Mg2Al4Zn3 phase, mp-1189454 in The Materials Project. https://next-gen.materialsproject.org/materials/mp-1189454?chemsys=Mg-Zn-Al.
[34] P. Tan, Z. Liu, J. Qin, Q. Wei, B. Wang, D. Yi, Enhanced corrosion performance by controlling grain boundary precipitates in a novel crossover Al-Cu-Zn-Mg alloy by optimizing Zn content, Mater. Charact. 208 (2024) 113615.
[35] Y.X. Liang, G.A. Li, L. Liu, J.T. Jiang, J. Cao, W.Z. Shao, L. Zhen, Corrosion behavior of Al-6.8Zn-2.2Mg-*Sc*-Zr alloy with high resistance to intergranular corrosion, J. Mater. Res. Technol. 24 (2023) 7552–7569.
[36] D.I. Udunwa, O.D. Onukwuli, S.C. Nwanonenyi, C.B. Ezekannagha, Novel imidazole based ionic liquid as anti-corrosion additive for aluminum alloy: combined experimental, DFT/MD simulation and soft computing approach, Appl. Surf. Sci. Adv. 19 (2024) 100578.
[37] N. Hajsafari, Z. Razaghi, S.H. Tabaian, Electrochemical study and molecular dynamics (MD) simulation of aluminum in the presence of garlic extract as a green inhibitor, J. Mol. Liq. 336 (2021) 116386.
[38] C. Han, M. Yu, J. Xiao, S. Li, J. Liu, Coupling effect on corrosion behavior of multi-phase AlCuMnFe IMPs in 2050-T84 Al-Li alloy, Corros. Sci. 223 (2023) 111462.
[39] Y. Dai, L. Yan, H. Wang, J. Hao, D. Yang, W. Li, J. Chang, H. Du, Effect of intermetallics on properties of Al-6.1Zn-2.3Mg-1.7Cu-0.15Zr-0.3Nd alloy: first-principles calculation, Mater. Today Commun 35 (2023) 106432.